

# Self-assembled structures from PEGylated polypeptide block copolymers synthesized using a combination of ATRP, ROP, and click chemistry

Cite this: *Soft Matter*, 2013, **9**, 11257

Po-Cheng Li, Yung-Chih Lin, Ming Chen and Shiao-Wei Kuo\*

In this study, we used a combination of atom transfer radical polymerization, ring opening polymerization, and click chemistry to synthesize new PEGylated polypeptide block copolymers of polystyrene-*b*-poly( $\gamma$ -propargyl-L-glutamate-*g*-ethylene oxide) [PS-*b*-(PPLG-*g*-MEO<sub>2</sub>)]. We employed Fourier transform infrared spectroscopy and wide-angle X-ray diffraction (WAXD) to determine the secondary structures of the  $\alpha$ -helical conformations of these PEGylated polypeptide block copolymers in the solid state, and circular dichroism spectroscopy to characterize them in solution. Hierarchical self-assembly of the PS-*b*-(PPLG-*g*-MEO<sub>2</sub>) diblock copolymers in the bulk state (characterized using WAXD, small-angle X-ray scattering, and transmission electron microscopy) led to the formation of lamellar structures as a result of microphase separation of the diblock copolymers; the hexagonal cylinder packing nanostructure featured  $\alpha$ -helical conformations of PEGylated polypeptide segments, which were oriented perpendicular to the director of the lamellar structure formed by the diblock copolymers. We obtained a range of micellar structures from the PS-*b*-(PPLG-*g*-MEO<sub>2</sub>) diblock copolymer in DMF (common solvent) upon the addition of selective solvents (H<sub>2</sub>O or MeCN). We observed only spherical micelles from the PS-*b*-(PPLG-*g*-MEO<sub>2</sub>) diblock copolymer in DMF–MeCN systems at all MeCN compositions. The micelle structures changed, however, from spherical structures to long wormlike, vesicles, and large compound micelles in the DMF–H<sub>2</sub>O system upon increasing the content of water. These different morphology transformations arose as a result of very different PS–solvent (H<sub>2</sub>O or MeCN) interaction parameters.

Received 30th July 2013  
Accepted 11th October 2013

DOI: 10.1039/c3sm52061g

[www.rsc.org/softmatter](http://www.rsc.org/softmatter)

## Introduction

Block copolymers attract considerable attention because of their abilities to self-assemble in the bulk state or in solution to form a range of different morphologies and sizes.<sup>1–5</sup> In the bulk state, diblock copolymers can form many different, well-defined, self-assembled nanostructures (*e.g.*, lamellar, gyroid, hexagonally packed cylindrical, and body-centered cubic micellar structures), depending on the relative volume fractions of the blocks, the total degree of polymerization, and the Flory–Huggins interaction parameter.<sup>6,7</sup> Diblock copolymers can also self-assemble spontaneously into well-defined micelles or aggregates [*e.g.*, spheres, rods, vesicles, and large compound micelles (LCMs)] in the presence of a selective solvent for one of the blocks, depending on, for example, the copolymer composition, the copolymer concentration, the nature of the common solvent, the amount of the selective solvent, the temperature, and the pH.<sup>8–10</sup>

Most of the amphiphilic diblock copolymers based on polystyrene (PS) blocks that have been used for nanofabrication—

including polystyrene-*b*-poly(4-vinylpyridine) (PS-*b*-P4VP),<sup>11,12</sup> polystyrene-*b*-polyvinylphenol (PS-*b*-PVPh),<sup>13–15</sup> polystyrene-*b*-polylactide (PS-*b*-PLA),<sup>16,17</sup> polystyrene-*b*-polyethyleneoxide (PS-*b*-PEO),<sup>18–20</sup> and poly(styrene-*b*-4-vinylbenzyl triazolymethyl methylthymine) (PS-*b*-PVBT)<sup>21</sup>—are organic–organic block copolymers with various functionalities. In addition, some organic–inorganic hybrid block copolymers [*e.g.*, polystyrene-*b*-polydimethylsiloxane (PS-*b*-PDMS)<sup>22</sup> and polystyrene-*b*-polyferrocenylsilane (PS-*b*-PFS)<sup>23</sup>] have also received attention for use in integrated circuit processing. Those studies, however, were focused only on PS-containing coil-based polymer chains. Rod–coil block copolymers comprise another important class of nanomaterials because of their potential uses in biological and optoelectronic applications;<sup>24–26</sup> here, the rod block segments are typically conjugated polymers,<sup>27,28</sup> liquid crystalline polymers,<sup>29,30</sup> and polypeptide segments.<sup>31,32</sup>

The rod segment of the block copolymer developed in this study was the polypeptide poly(L-glutamate). This polypeptide forms hierarchically ordered structures with  $\alpha$ -helical rod-like secondary structures (stabilized through intramolecular hydrogen bonds) and  $\beta$ -sheet secondary structures (stabilized through intermolecular hydrogen bonds).<sup>33</sup> For several decades,

Department of Materials and Optoelectronic Science, National Sun Yat-Sen University, Kaohsiung, 804, Taiwan. E-mail: kuosw@faculty.nsysu.edu.tw

most methods for synthesizing poly(peptide-*b*-nonpeptide) (rod-coil) block copolymers<sup>34–36</sup> have involved the nonpeptide blocks [e.g., PS,<sup>37</sup> PEO,<sup>38</sup> poly(*N*-isopropylacrylamide),<sup>39</sup> and poly(2-ethyl-2-oxazoline)<sup>40</sup>] functioning as macroinitiators. Using Fourier transform infrared (FTIR) spectroscopy, Klok *et al.* found that poly(styrene-*b*- $\gamma$ -benzyl-L-glutamate) (PS-*b*-PBLG) copolymers featured significantly stabilized  $\alpha$ -helical secondary structures relative to those of corresponding PBLG oligomers.<sup>37</sup>

The presence of benzene rings in PBLG is often problematic when designing water-soluble  $\alpha$ -helical polypeptides because it might result in structures exhibiting low water-solubility.<sup>41</sup> To overcome their low water-solubility, Cheng *et al.* prepared polypeptides with long side chains bearing charged groups through thiol-ene click reactions of a  $\gamma$ -(4-allyloxybenzyl)-L-glutamate *N*-carboxyanhydride monomer; these systems were highly water-soluble and highly helical, even when the degree of polymerization (DP) was as low as 10.<sup>42</sup> Nevertheless, polyelectrolytes featuring charged peptide residues will display pH-dependent solubility and limited circulation lifetimes as a result of aggregation with oppositely charged biopolymers.<sup>43</sup> Nonionic yet water-soluble polypeptides featuring stable  $\alpha$ -helical conformations are, therefore, attractive materials for biomedical applications. The grafting of polyethyleneglycol (PEG) onto a polypeptide through direct modification of a peptide *N*-carboxyanhydride monomer to form the PEGylated polypeptide is the method typically used to improve the behavior of the polypeptide *in vivo*.<sup>44</sup> Deming *et al.* prepared the first examples of nonionic, water-soluble, PEG-functionalized polylysines.<sup>45</sup> In addition, the attachment of azide-terminated PEG to poly( $\gamma$ -propargyl-L-glutamate) (PPLG) through click reactions is a highly efficient means of grafting PEG moieties onto a polypeptide side chain and maintaining its  $\alpha$ -helical conformation.<sup>45,46</sup> In this study, we used atom transfer radical polymerization (ATRP), ring opening polymerization (ROP), and click chemistry to combine several advantageous features—self-assembly (microphase separation) of diblock copolymers, water-soluble PEO side chains, and helical polypeptides—into the same polymer chain. First, we synthesized a PS derivative through ATRP using (1-bromoethyl)benzene as the initiator and then treated it with NaN<sub>3</sub> to obtain the azido-terminated PS, which we reduced (PPh<sub>3</sub> in THF-water) to the primary amino-terminated PS macroinitiator (PS-NH<sub>2</sub>). Next, we prepared polystyrene-*b*-poly( $\gamma$ -propargyl-L-glutamate) (PS-*b*-PPLG) copolymers through ROP of the monomer  $\gamma$ -propargyl-L-glutamate *N*-carboxyanhydride (PLG-NCA), using PS-NH<sub>2</sub> as the macroinitiator. Finally, we used click reactions to synthesize amphiphilic PS-*b*-(PPLG-*g*-MEO<sub>2</sub>) copolymers from 1-(2-methoxyethoxy)-2-azidoethane (MEO<sub>2</sub>-N<sub>3</sub>) and PS-*b*-PPLG. Scheme 1 summarizes all these reactions. We used wide-angle X-ray diffraction (WAXD), small-angle X-ray scattering (SAXS), FTIR spectroscopy, circular dichroism (CD) spectroscopy, transmission electron microscopy (TEM), and dynamic light scattering (DLS) to analyze the hierarchical self-assembled structures formed from PS-*b*-(PPLG-*g*-MEO<sub>2</sub>) diblock copolymers in the bulk and in solution as well as their secondary structures.

## Experiments

### Materials

Styrene (Aldrich) was vacuum-distilled over CaH<sub>2</sub> and stored under N<sub>2</sub> at -10 °C. 2-(2-Methoxyethoxy)ethanol (MEO<sub>2</sub>OH, Sigma) was used without further purification. Propargyl alcohol and L-glutamic acid were purchased from Tokyo Kasei Kogyo. Copper(i) bromide (CuBr) was purified by washing with glacial AcOH overnight, followed by washing with absolute EtOH and ethyl ether and then drying under vacuum. *N,N*-Dimethylformamide (DMF), NaN<sub>3</sub>, triethylamine (TEA), 1-phenylethyl bromide, trichloro[4-(chloromethyl)phenyl]silane, PPh<sub>3</sub>, and *N,N,N',N',N''*-pentamethyldiethylenetriamine (PMDETA, 99%) were purchased from Aldrich. All solvents were distilled prior to use. Monoazide-functionalized MEO<sub>2</sub>,  $\gamma$ -propargyl-L-glutamate, and PS-*b*-PPLG were prepared according to previous literature procedures.<sup>47–51</sup>

### 2-(2-Methoxyethoxy)ethyl tosylate

A solution of TsCl (10.2 g, 49.9 mmol) in a small quantity of CH<sub>2</sub>Cl<sub>2</sub> was added to a solution of Et<sub>3</sub>N (8.7 mL) and MEO<sub>2</sub>OH (5.00 g, 41.6 mmol) in CH<sub>2</sub>Cl<sub>2</sub> (50 mL). The resulting solution was stirred under Ar overnight. Saturated aqueous NaHCO<sub>3</sub> (50 mL) was added and then the organic phase was washed sequentially with deionized water (50 mL) and saturated aqueous NaHCO<sub>3</sub> (50 mL), dried (MgSO<sub>4</sub>), and concentrated (rotavap) to produce an oily liquid (10.8 g, 95%).

### 2-(2-Methoxyethoxy)ethyl azide (MEO<sub>2</sub>-N<sub>3</sub>)

2-(2-Methoxyethoxy)ethyl tosylate (5.00 g, 18.2 mmol) added *via* a syringe to a suspension of NaN<sub>3</sub> (1.77 g, 27.3 mmol) in DMF (30 mL) and then the mixture was stirred at 50 °C overnight under N<sub>2</sub>. The mixture was diluted with a large amount of water and extracted with diethyl ether. The organic phase was washed with water, dried (MgSO<sub>4</sub>), and concentrated (rotavap) to yield an oil (2.5 g, 96%).

### PEGylated polypeptide block copolymers [PS-*b*-(PPLG-*g*-MEO<sub>2</sub>)] *via* click chemistry

MEO<sub>2</sub>-N<sub>3</sub> (0.340 g, 2.40 mmol), PS-*b*-PPLG (0.200 g, 1.20 mmol), and CuBr (0.170 g, 1.18 mmol) were dissolved in DMF (25 mL) in a flask equipped with a magnetic stirrer bar. After one brief freeze-thaw-pump cycle, PMDETA (24.6  $\mu$ L, 1.18 mmol) was added. The reaction mixture was then carefully degassed through three freeze-thaw-pump cycles, placed in an oil bath thermostatted at 60 °C, and stirred for 24 h. After evaporating all of the solvent under reduced pressure, the residue was dissolved in THF and passed through a neutral alumina column to remove the copper catalyst. The THF was evaporated and the product was precipitated using MeOH. The resulting polymer was filtered and dried under vacuum at room temperature, yielding PS-*b*-(PPLG-*g*-MEO<sub>2</sub>) as a white powder.

### Micelle solutions

The PS-*b*-(PPLG-*g*-MEO<sub>2</sub>) diblock copolymer was first dissolved in DMF, a common solvent for both PS and PPLG-*g*-MEO<sub>2</sub>

blocks. A second solvent (water or MeCN) was added slowly to the stirred polymer solution, *via* a syringe pump, at a constant rate (typically 1–5 mL h<sup>-1</sup>). To estimate the ideal solvent composition for the formation of micelles, addition of solvent was continued until the solution turned turbid during the first trial. In subsequent experiments, addition was stopped prior to the appearance of turbidity. Stirring of the solution was continued for 2 days before further characterization.

### Characterization

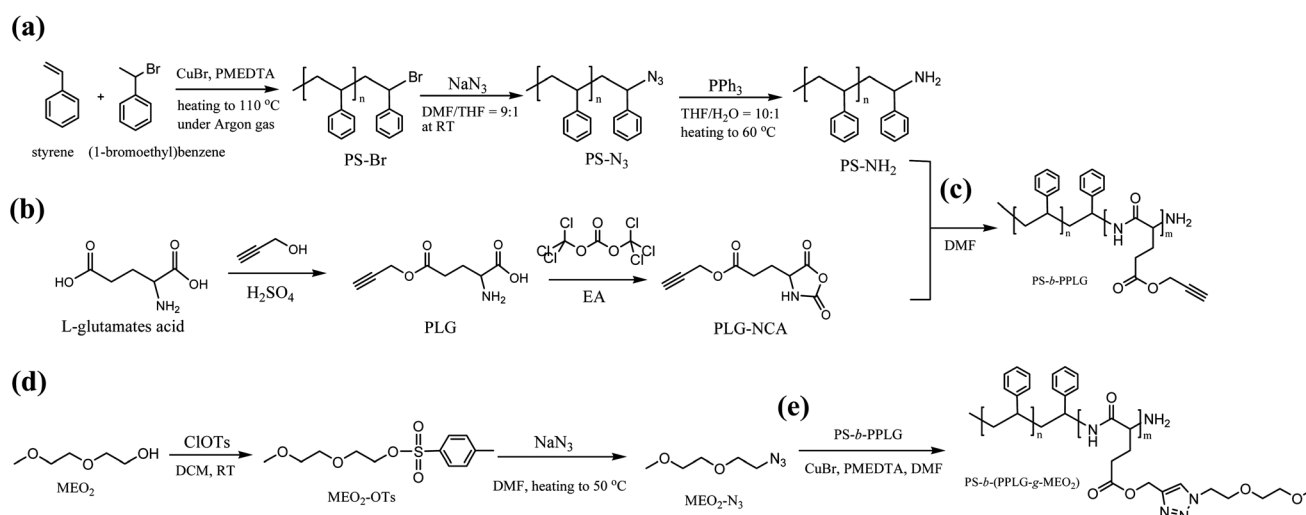
<sup>1</sup>H NMR spectra were recorded at room temperature using a Bruker AM 500 (500 MHz) spectrometer, with the residual proton resonance of the deuterated solvent acting as the internal standard. Molecular weights and molecular weight distributions were determined through gel permeation chromatography (GPC) using a Waters 510 high-performance liquid chromatograph equipped with a 410 differential refractometer and three Ultrastaygel columns (100, 500, and 10<sup>3</sup> Å) connected in series, with DMF as the eluent (flow rate: 0.4 mL min<sup>-1</sup>). Differential scanning calorimetry (DSC) was performed using a TA-Q20 instrument operated at a scan rate of 20 °C min<sup>-1</sup> over a temperature range from -90 to 200 °C under a N<sub>2</sub> atmosphere. FTIR spectra of the polymer films were recorded using the conventional KBr disk method. The films used in this study were sufficiently thin to obey the Beer-Lambert law. FTIR spectra were recorded using a Bruker Tensor 27 FTIR spectrophotometer; 32 scans were collected at a spectral resolution of 1 cm<sup>-1</sup>. IR spectra recorded at elevated temperatures were obtained by using a cell mounted inside the temperature-controlled compartment of the spectrometer. CD spectra were recorded using a JASCO J-810 spectrometer and samples were dissolved in MeOH at a concentration of 1 mg mL<sup>-1</sup>. X-ray diffraction (XRD) data were collected using the wiggler beamline BL17A1 of the National Synchrotron Radiation Research Center (NSRRC), Taiwan. A triangular bent Si (111) single crystal was employed to obtain a monochromated beam with a

wavelength ( $\lambda$ ) of 1.33001 Å. SAXS experiments were performed using the SWAXS instrument at the BL17B3 beamline of the NSRRC, Taiwan; the X-ray beam had a diameter of 0.5 mm and a wavelength ( $\lambda$ ) of 1.24 Å. The samples (thickness: 1 mm) were sealed between two thin Kapton windows (thickness: 80  $\mu$ m) and analyzed at room temperature. TEM images were recorded using a JEOL-2100 transmission electron microscope operated at an accelerating voltage of 200 kV. Ultrathin sections of the TEM samples (thickness: *ca.* 70 nm) in the bulk state were prepared using a Leica Ultracut UCT microtome equipped with a diamond knife. For TEM studies in solution, a drop of the resulting micelle solution was sprayed onto a Cu TEM grid covered with a Formvar supporting film that had been pre-coated with a thin film of carbon. All samples were left to dry at room temperature for 1 day prior to observation. After 1 min, the excess solvent was blotted away using a strip of filter paper. All samples were stained with ruthenium tetroxide (RuO<sub>4</sub>), which generally results in PS blocks appearing dark.

## Results and discussion

### Synthesis of PS-*b*-(PPLG-*g*-MEO<sub>2</sub>) through click reaction of PS-*b*-PPLG with MEO<sub>2</sub>-N<sub>3</sub>

Fig. 1 presents the <sup>1</sup>H NMR spectra of PS-NH<sub>2</sub>, PS-*b*-PPLG, and PS-*b*-(PPLG-*g*-MEO<sub>2</sub>). The <sup>1</sup>H NMR spectrum of the PS-NH<sub>2</sub> macroinitiator in CDCl<sub>3</sub> features signals at 6.40–7.23 and 1.20–2.50 ppm corresponding to the aromatic (protons 4) and aliphatic CH<sub>2</sub>CH(Ph) (protons 2 and 3) protons, respectively. We assigned the singlet at 3.49 ppm to the methine proton adjacent to the terminal PS amino group. Fig. 1(b) displays the <sup>1</sup>H NMR spectrum of PS<sub>235</sub>-*b*-PPLG<sub>57</sub> in CDCl<sub>3</sub> and 15 wt% TFA. The signal for the proton on the nitrogen atom of PPLG appeared as a singlet at 7.95 ppm; the singlets at 2.50 and 4.78 ppm corresponded to the HC≡C-C and C≡C-CH<sub>2</sub> protons, respectively. The signals of the PS block appeared at 1.30–1.98 [CH<sub>2</sub>CH(Ph)], 3.49 [CH(Ph)NH], and 6.38–7.23 (phenyl protons of PS) ppm. We



**Scheme 1** Syntheses of (a) the PS-NH<sub>2</sub> homopolymer, (b) PLG-NCA, (c) the PS-*b*-PPLG diblock copolymer through NCA ROP polymerization from PS-NH<sub>2</sub> and PLG-NCA, (d) MEO<sub>2</sub>-N<sub>3</sub>, and (e) the PS-*b*-(PPLG-*g*-MEO<sub>2</sub>) diblock copolymer through the click reaction of PS-*b*-PPLG and MEO<sub>2</sub>-N<sub>3</sub>.

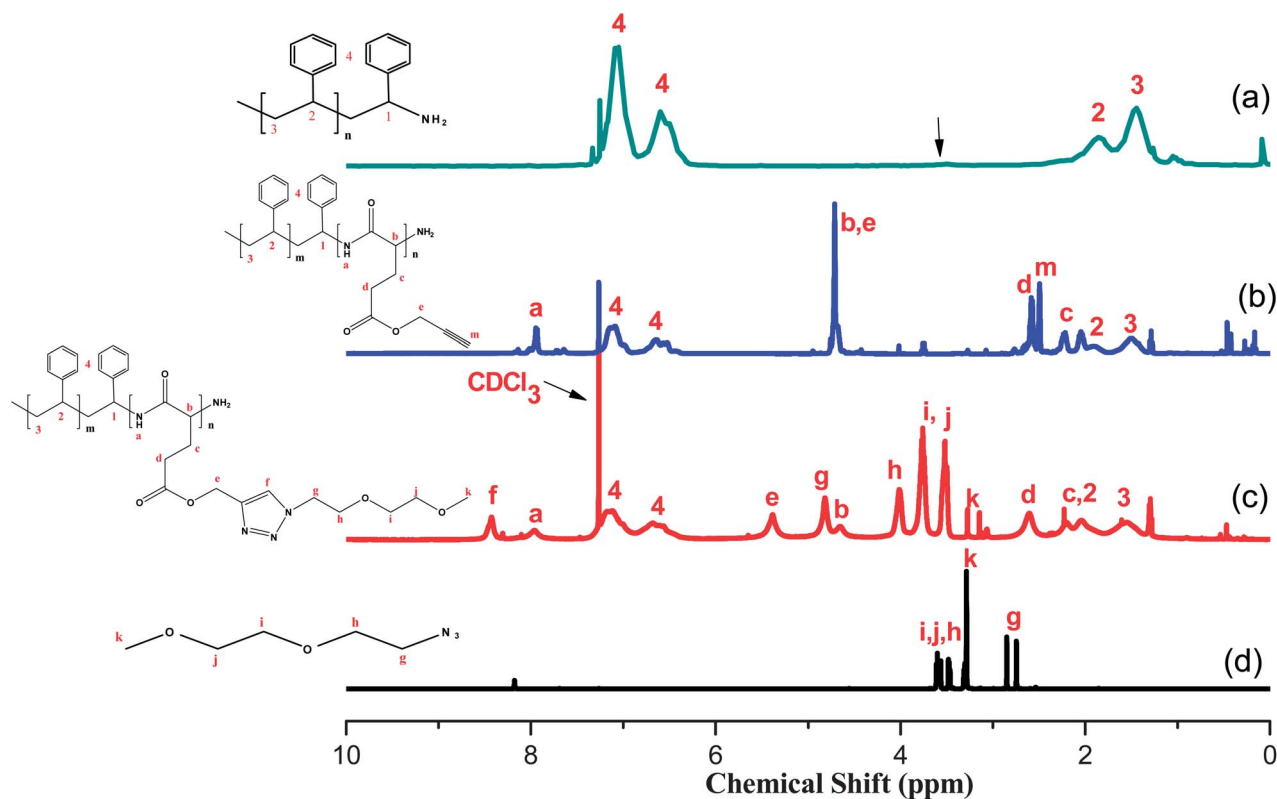


**Fig. 1**  $^1\text{H}$  NMR spectra of (a)  $\text{PS}_{235}\text{-NH}_2$  in  $\text{CDCl}_3$ , (b)  $\text{PS}_{235}\text{-}b\text{-PPLG}_{57}$  in  $\text{CDCl}_3\text{-TFA}$ , (c)  $\text{PS}_{235}\text{-}b\text{-(PPLG-g-MEO}_2\text{)}_{57}$  in  $\text{CDCl}_3\text{/TFA}$ , and (d)  $\text{MEO}_2\text{-N}_3$  in  $\text{CDCl}_3$ .

determined the molar masses of the  $\text{PS-}b\text{-PPLG}$  copolymers from their  $^1\text{H}$  NMR spectra.<sup>50</sup> The signal at 2.83 ppm for the  $\text{CH}_2$  group connected to the azide unit of  $\text{MEO}_2\text{-N}_3$  shifted

downfield significantly (to 4.82 ppm) for  $\text{PS-}b\text{-(PPLG-g-MEO}_2\text{)}$ . In addition, the signals for the other  $\text{CH}_2$  and  $\text{CH}_3$  groups of  $\text{MEO}_2\text{-N}_3$  appeared near 3.27, 3.50, 3.75, and 4.00 ppm. The

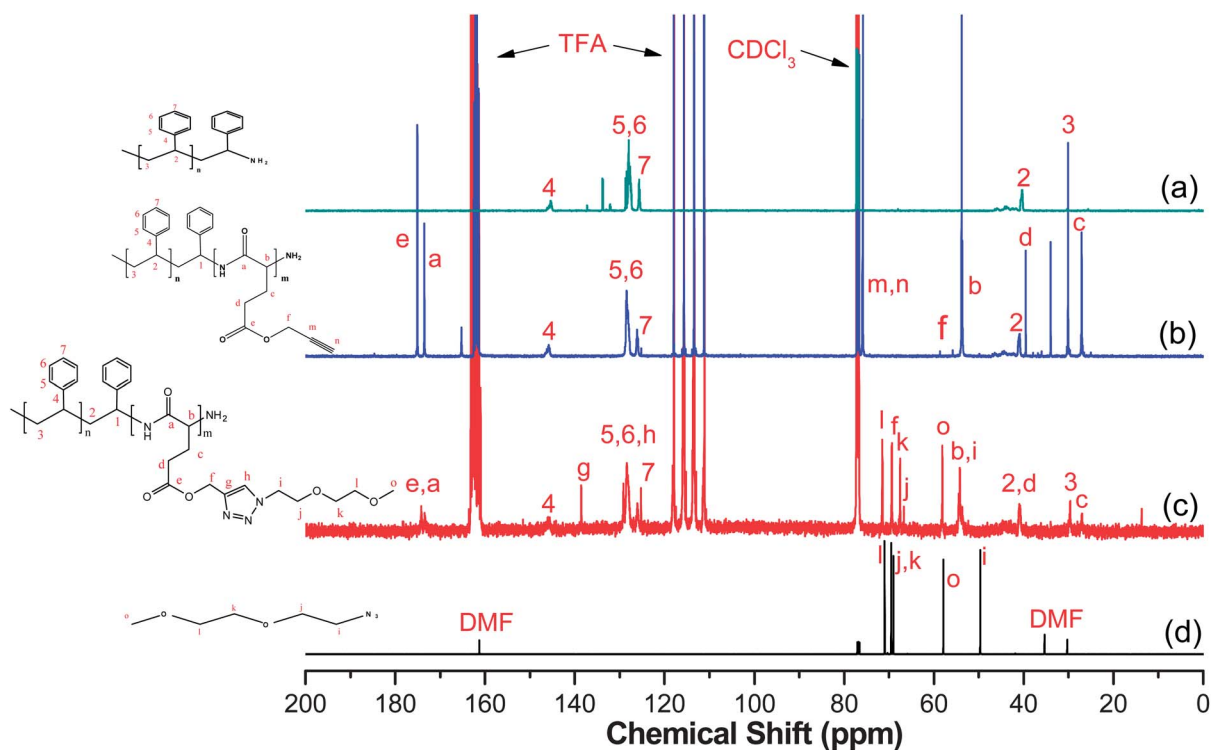


**Fig. 2**  $^{13}\text{C}$  NMR spectra of (a)  $\text{PS}_{235}\text{-NH}_2$  in  $\text{CDCl}_3$ , (b)  $\text{PS}_{235}\text{-}b\text{-PPLG}_{57}$  in  $\text{CDCl}_3\text{/TFA}$ , (c)  $\text{PS}_{235}\text{-}b\text{-(PPLG-g-MEO}_2\text{)}_{57}$  in  $\text{CDCl}_3\text{/TFA}$ , and (d)  $\text{MEO}_2\text{-N}_3$  in  $\text{CDCl}_3$ .

proton on the nitrogen atom of PPLG resonated as a singlet at 7.95 ppm. The resonance at 8.43 ppm was due to the protons of the triazole structures formed through the click reactions, confirming the successful synthesis of PS-*b*-(PPLG-*g*-MEO<sub>2</sub>) diblock copolymers.

Fig. 2 presents the <sup>13</sup>C NMR spectra of PS-NH<sub>2</sub>, PS-*b*-PPLG, PS-*b*-(PPLG-*g*-MEO<sub>2</sub>), and MEO<sub>2</sub>-N<sub>3</sub>; the C=O and amide carbon atom signals appeared in the <sup>13</sup>C NMR spectrum of PS-*b*-(PPLG-*g*-MEO<sub>2</sub>) at 173.5 and 175.0 ppm, respectively, while those of the CH<sub>2</sub> and CH<sub>3</sub> from MEO<sub>2</sub>-N<sub>3</sub> appeared at 54.1, 57.9, 66.5, 67.6, and 71.5 ppm. The signals for the CH<sub>2</sub> group connected to the azide unit of MEO<sub>2</sub>-N<sub>3</sub> (49.3 ppm) shifted downfield significantly to 54.1 ppm for the PS-*b*-(PPLG-*g*-MEO<sub>2</sub>) diblock copolymer. The signal of the alkyne carbon atoms of PPLG (originally at 73.4 ppm) disappeared, but two new peaks appeared at 126.0 and 138.1 ppm, representing the carbon atoms of the triazole structures resulting from the click reaction, confirming the successful synthesis of PS-*b*-(PPLG-*g*-MEO<sub>2</sub>) diblock copolymers with close to 100% grafting. FTIR spectroscopic analysis also confirmed the complete disappearance of the characteristic signals for the azido and acetylenic groups (Fig. 3). The signal at 2107 cm<sup>-1</sup>, corresponding to the absorbance of the azido group of MEO<sub>2</sub>-N<sub>3</sub>, and the signal at 2130 cm<sup>-1</sup>, corresponding to the acetylenic group of PS-*b*-PPLG, were absent in the spectrum of PS-*b*-(PPLG-*g*-MEO<sub>2</sub>). The absorption bands of the ether (C-O-C) groups of the EO moiety (at 1110 cm<sup>-1</sup>) and the amide I groups of PS-*b*-PPLG (at 1657 cm<sup>-1</sup>) appeared in the spectrum of the PS-*b*-(PPLG-*g*-MEO<sub>2</sub>) diblock copolymer, indicating that the azido and acetylene functionalities had participated in the click reaction. Fig. 4 displays GPC traces of the PS-NH<sub>2</sub> macroinitiator, PS-*b*-PPLG, and PS-*b*-(PPLG-*g*-MEO<sub>2</sub>); each reveals a narrow molecular weight distribution (<1.1). Block copolymers prepared from the PS macroinitiator resulted in products with narrow polydispersity and high symmetry, with monomodal GPC traces. The absence of the PS-NH<sub>2</sub> macroinitiator peak supports the formation of the PS-*b*-PPLG diblock copolymers, with the peak maxima of these spectra clearly shifting to higher molecular

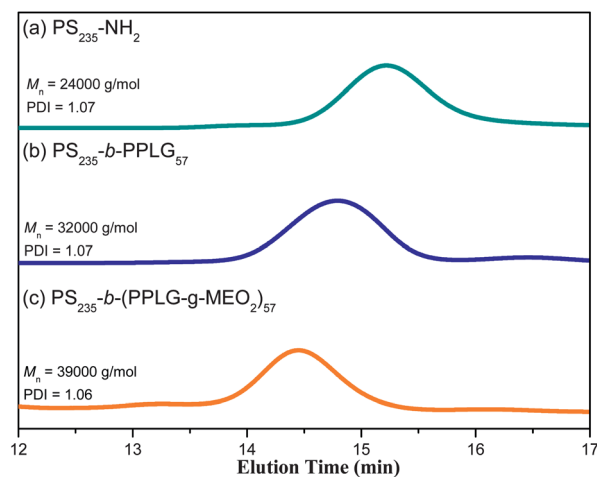


Fig. 4 GPC traces of (a) the macroinitiator PS<sub>235</sub>-NH<sub>2</sub>, (b) PS<sub>235</sub>-*b*-PPLG<sub>57</sub>, and (c) PS<sub>235</sub>-*b*-(PPLG-*g*-MEO<sub>2</sub>)<sub>57</sub>.

Table 1 Molecular characteristics of the PS homopolymer and the PS-*b*-PPLG and PS-*b*-(PPLG-*g*-MEO<sub>2</sub>) block copolymers

Sample	M <sub>n</sub> <sup>a</sup>	M <sub>n</sub> <sup>b</sup>	PDI <sup>b</sup>	PS (wt%)	PS <sup>c</sup> (vol%)	T <sub>g</sub> <sup>d</sup> (°C)
PS <sub>235</sub> -NH <sub>2</sub>	24 440	24 000	1.07	100	100	104
PS <sub>235</sub> - <i>b</i> -PPLG <sub>57</sub>	33 960	32 000	1.07	71.9	78.2	104/13
PS <sub>235</sub> - <i>b</i> -(PPLG- <i>g</i> -MEO <sub>2</sub> ) <sub>57</sub>	42 160	39 000	1.06	57.9	66.6	104/-6
PS <sub>235</sub> - <i>b</i> -PPLG <sub>106</sub>	42 140	38 000	1.10	57.9	65.8	104/16
PS <sub>235</sub> - <i>b</i> -(PPLG- <i>g</i> -MEO <sub>2</sub> ) <sub>106</sub>	57 400	53 000	1.11	42.6	51.7	104/-2

<sup>a</sup> Determined from <sup>1</sup>H NMR spectra. <sup>b</sup> Determined from GPC analysis. <sup>c</sup> Determined using the group contribution method to calculate the density. <sup>d</sup> Determined from DSC analysis.

weights for the PS-*b*-PPLG and PS-*b*-(PPLG-*g*-MEO<sub>2</sub>) diblock copolymers. Table 1 lists the molecular weights and thermal properties of the PS-NH<sub>2</sub>, PS-*b*-PPLG, and PS-*b*-(PPLG-*g*-MEO<sub>2</sub>) diblock copolymers prepared in this study, as determined through GPC, <sup>1</sup>H NMR spectroscopy, and DSC analyses.

### Thermal analyses of PS-*b*-(PPLG-*g*-MEO<sub>2</sub>) copolymers

Fig. 5 presents DSC thermograms of the PS-NH<sub>2</sub>, PS-*b*-PPLG, and PS-*b*-(PPLG-*g*-MEO<sub>2</sub>) block copolymers. During the second heating run of the PS-*b*-PPLG copolymer, we observed [Fig. 5(b)] two glass transition temperatures (T<sub>g</sub>, at ca. 104 and 13 °C) representing the PS [Fig. 5(a)] and PPLG block segments, respectively; that is, phase separation occurred in the PS-*b*-PPLG copolymers. After grafting the MEO<sub>2</sub> moiety onto PS-*b*-PPLG, the value of T<sub>g</sub> of the PS block segment did not change, but we observed dramatic changes in the second-heating-run DSC trace.

The glass transition temperature of the peptide segment in PS-*b*-(PPLG-*g*-MEO<sub>2</sub>) decreased significantly, to approximately -6 °C; the value of T<sub>g</sub> for the peptide segment of PS-*b*-(PPLG-*g*-MEO<sub>2</sub>) was lower (by ca. 19 °C) than that of the corresponding PS-*b*-PPLG copolymer. This decrease in the value of T<sub>g</sub> of PS-*b*-(PPLG-*g*-MEO<sub>2</sub>) was due to the effect of the side chain increasing the free volume and, thereby, effectively increasing the molecular chain motion.

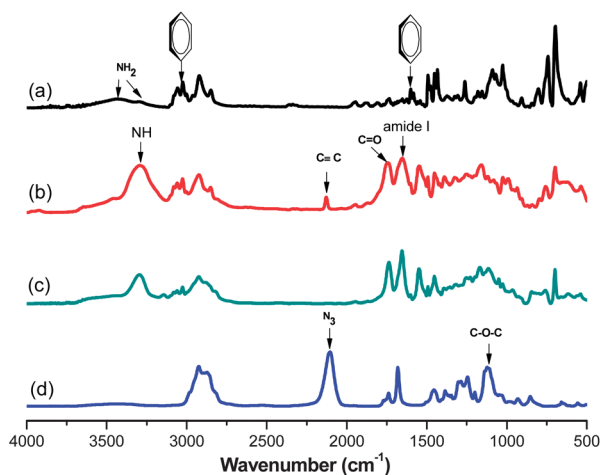
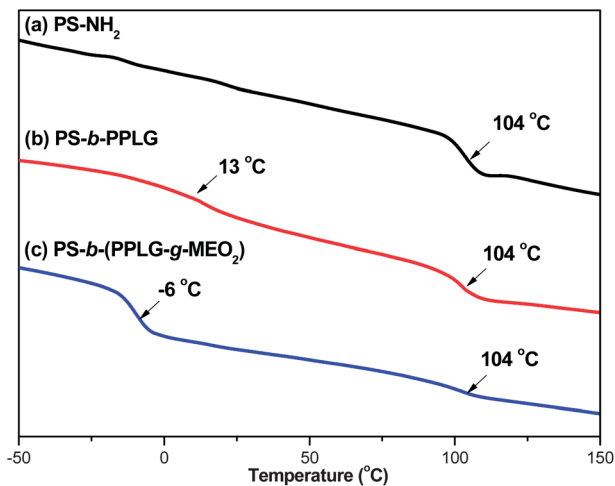


Fig. 3 FTIR spectra of (a) PS<sub>235</sub>-NH<sub>2</sub>, (b) PS<sub>235</sub>-*b*-PPLG<sub>57</sub>, (c) PS<sub>235</sub>-*b*-(PPLG-*g*-MEO<sub>2</sub>)<sub>57</sub>, and (d) MEO<sub>2</sub>-N<sub>3</sub>.



**Fig. 5** DSC traces (second heating) of (a)  $PS_{235}\text{-NH}_2$ , (b)  $PS_{235}\text{-}b\text{-PPLG}_{57}$ , and (c)  $PS_{235}\text{-}b\text{-}(\text{PPLG-g-MEO}_2)_{57}$ .

### Using FTIR and CD spectroscopy and WAXD to study the conformation of the PEGylated peptide segment

We recorded FTIR spectra at room temperature to obtain information relating to the conformation of the peptide segments in the  $PS\text{-}b\text{-PPLG}$  and  $PS\text{-}b\text{-}(\text{PPLG-g-MEO}_2)$  block copolymers (Fig. 6). For PPLG, the amide I band at  $1655\text{ cm}^{-1}$  is characteristic of the  $\alpha$ -helical secondary structure; for PPLG possessing a  $\beta$ -sheet conformation, the position of the amide I band should shift to  $1627\text{ cm}^{-1}$ , the free C=O group of the side chain group of PPLG should appear as a band at  $1744\text{ cm}^{-1}$ , and a signal at  $1600\text{ cm}^{-1}$  should appear corresponding to the benzene ring stretching of the PS segments.<sup>50</sup> Clearly, the spectra of the  $PS_{235}\text{-}b\text{-PPLG}_{57}$  and  $PS_{235}\text{-}b\text{-PPLG}_{106}$  block copolymers featured signals for only the  $\alpha$ -helical conformation at  $1655\text{ cm}^{-1}$ ; no signals were present for the  $\beta$ -sheet conformation at  $1627\text{ cm}^{-1}$ . This result is similar to that reported by Papadopoulos *et al.* for PBLG.<sup>33</sup> At low degrees of polymerization (DP; <18 for PBLG), both secondary structures are present; as the DP increases, however, the  $\alpha$ -helical secondary structure is favored.<sup>33</sup>

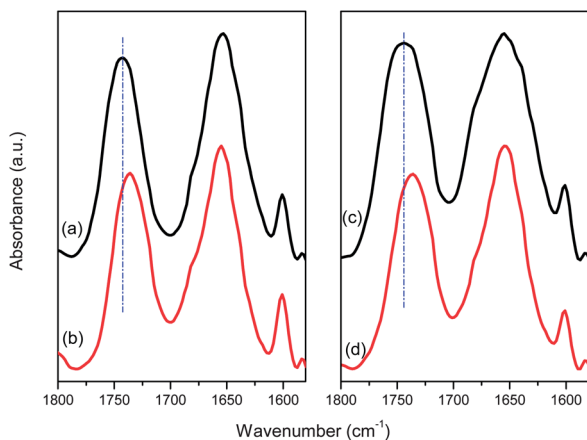


**Fig. 6** FTIR spectra of (a)  $PS_{235}\text{-}b\text{-PPLG}_{57}$ , (b)  $PS_{235}\text{-}b\text{-}(\text{PPLG-g-MEO}_2)_{57}$ , (c)  $PS_{235}\text{-}b\text{-PPLG}_{106}$ , and (d)  $PS_{235}\text{-}b\text{-}(\text{PPLG-g-MEO}_2)_{106}$  at room temperature.

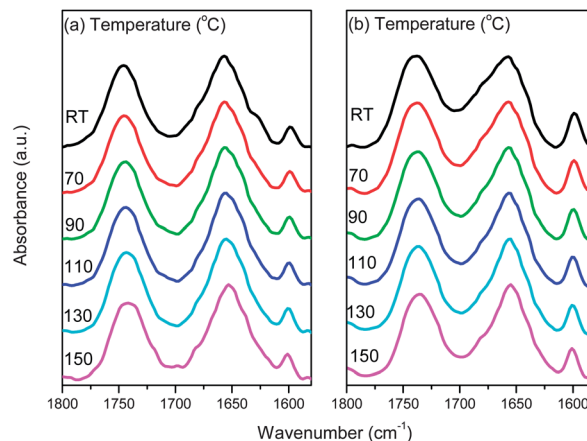


**Fig. 7** FTIR spectra of (a)  $PS_{235}\text{-}b\text{-PPLG}_{57}$  and (b)  $PS_{235}\text{-}b\text{-}(\text{PPLG-g-MEO}_2)_{57}$  at various temperatures.

After performing the click reactions, the signal of the free C=O group of the side chain group of PPLG shifted to  $1735\text{ cm}^{-1}$  for the  $PS\text{-}b\text{-}(\text{PPLG-g-MEO}_2)$  copolymers, also indicating that the successful grafting of the EO segment affects the chemical environment of the side chain groups of PPLG. In addition, the  $PS\text{-}b\text{-}(\text{PPLG-g-MEO}_2)$  copolymers obtained after performing the click reactions also featured only  $\alpha$ -helical secondary structures (signal at  $1655\text{ cm}^{-1}$ ). We recorded

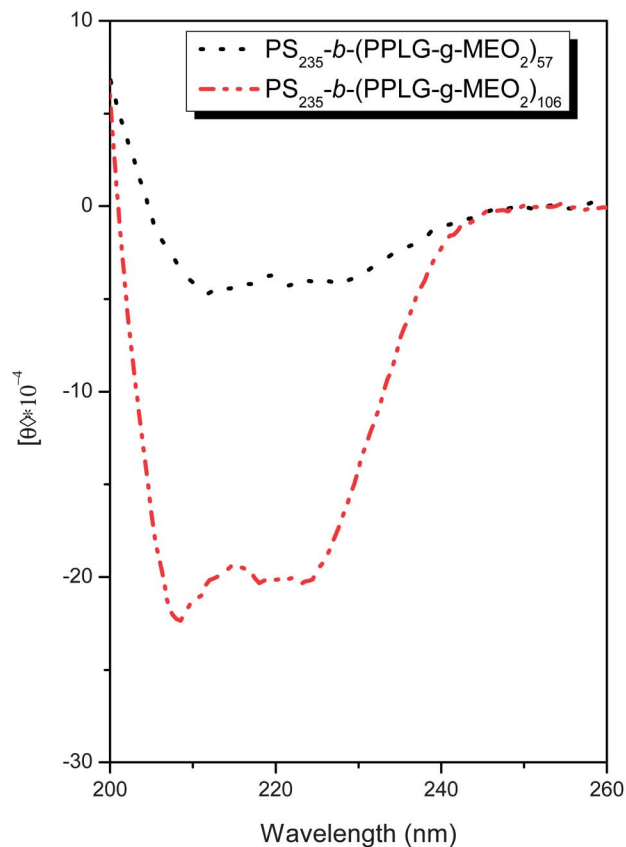


**Fig. 8** CD spectra of (a)  $PS_{235}\text{-}b\text{-}(\text{PPLG-g-MEO}_2)_{57}$  and  $PS_{235}\text{-}b\text{-}(\text{PPLG-g-MEO}_2)_{106}$  in MeOH ( $1.0\text{ mg mL}^{-1}$ ).

temperature-dependent FTIR spectra to obtain information relating to the conformation of the peptide segment (Fig. 7). The FTIR spectra of the PS-*b*-PPLG and PS-*b*-(PPLG-*g*-MEO<sub>2</sub>) copolymers at various temperatures revealed that the  $\alpha$ -helical secondary structures were significantly stabilized, remaining almost unchanged upon increasing the temperature. We also recorded CD spectra to quantify the behavior of the secondary structures of the PS-*b*-(PPLG-*g*-MEO<sub>2</sub>) block copolymers dissolved in MeOH (Fig. 8). The  $\alpha$ -helical structure was characterized by a triply inflected spectrum, corresponding to two negative bands at 208 and 222 nm. The  $\beta$ -sheet structure was characterized by a negative minimum band near 218 nm and the random coil structure was characterized by a small positive band at 218 nm and a large negative band near 200 nm.<sup>51,52</sup> The solutions of both of the PS-*b*-(PPLG-*g*-MEO<sub>2</sub>) copolymers in MeOH displayed negative bands at 208 and 222 nm, corresponding to an  $\alpha$ -helical structure for each of these two diblock copolymers. Furthermore, the widths of the amide I signals of the PS-*b*-(PPLG-*g*-MEO<sub>2</sub>) ( $W_{1/2} = 38 \text{ cm}^{-1}$ ) copolymers were much narrower than those of the PS-*b*-PPLG ( $W_{1/2} = 53 \text{ cm}^{-1}$ ) copolymers, indicating more order in the hexagonal cylinder packing of the  $\alpha$ -helical secondary structure for the PS-*b*-(PPLG-*g*-MEO<sub>2</sub>) copolymers.

We also used WAXD (recorded at 393 K) to characterize the secondary structural changes of the PS-*b*-PPLG and

PS-*b*-(PPLG-*g*-MEO<sub>2</sub>) systems (Fig. 9). The diffraction pattern of PS-*b*-PPLG reveals [Fig. 9(a)] the presence of an  $\alpha$ -helical secondary structure. The first peak at a value of  $q$  of 0.53 represents the inter-cylinder distance ( $d = 1.18 \text{ nm}$ ). The two weaker reflections at higher angles, with positions  $1 : 3^{1/2} : 4^{1/2}$  relative to the primary peak ( $q^*$ ), are indexed according to the (10), (11), and (20) reflections of a two-dimensional (2D) short range order of hexagonal packing of cylinders composed of 18/5  $\alpha$ -helices with a cylinder distance of 1.18 nm.<sup>49</sup> The WAXD patterns of the PS-*b*-(PPLG-*g*-MEO<sub>2</sub>) copolymers [Fig. 9(b)] differed from those of the PS-*b*-PPLG copolymers. After the click reactions, the patterns of the PS-*b*-(PPLG-*g*-MEO<sub>2</sub>) copolymers revealed much higher order for their  $\alpha$ -helical secondary structures than those of the PS-*b*-PPLG copolymers, with a much narrower and sharper first peak at a value of  $q$  of 0.4 representing the inter-cylinder distance ( $d = 1.58 \text{ nm}$ ) and the two stronger reflections at higher angles, with positions  $1 : 3^{1/2} : 4^{1/2}$ . In general, graft or bottlebrush copolymers are comblike macromolecules with highly densely grafted polymeric branches. The repulsive force between the adjacent branches of the MEO<sub>2</sub> moiety is believed to cause the backbone to stretch out, resulting in rigid cylindrical polymers, and a much higher order in WAXD and FTIR spectroscopic analyses, when the backbone is much longer than the branches.<sup>53,54</sup> Structurally speaking, we also would expect the incorporation of the MEO<sub>2</sub> moieties into the PPLG side chains to expand or swell the distance between the 2D hexagonally packed cylinders of  $\alpha$ -helices of PPLG-*g*-MEO<sub>2</sub> from 1.18 to 1.58 nm.<sup>49</sup>

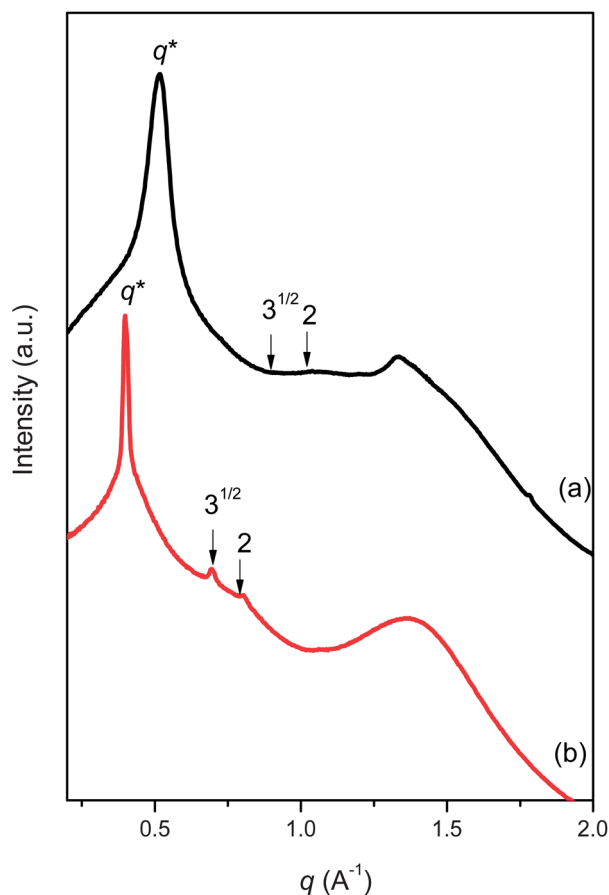


**Fig. 9** WAXD patterns (a) PS<sub>235</sub>-*b*-PPLG<sub>106</sub> and (b) PS<sub>235</sub>-*b*-(PPLG-*g*-MEO<sub>2</sub>)<sub>106</sub> at 393 K.

### Self-assembled structures of PS-*b*-(PPLG-*g*-MEO<sub>2</sub>) copolymers in the bulk state

To observe the structures formed through the self-assembly of the hexagonally packed block polypeptides, we conducted SAXS analyses of the PS-*b*-PPLG and PS-*b*-(PPLG-*g*-MEO<sub>2</sub>) systems at room temperature. In Fig. 10(a) and (c) we observe lamellar structures for both PS<sub>235</sub>-*b*-PPLG<sub>57</sub> and PS<sub>235</sub>-*b*-PPLG<sub>106</sub> with the maximum intensity appearing at values of  $q^*$  of approximately  $0.032 \text{ nm}^{-1}$  ( $d = 19.57 \text{ nm}$ ) and  $0.0186 \text{ nm}^{-1}$  ( $d = 33.70 \text{ nm}$ ), respectively, with the second reflections appearing at  $2q^*$ . Developed from a combination of both the WAXD and SAXS data, Scheme 2(A) presents a possible hierarchical packing model for the PS-*b*-PPLG rod-coil diblock copolymers. The PPLG block forms a rigid rod with an inter-cylinder diameter of 1.18 nm, while the PS block forms a coil. This diblock copolymer self-assembles into a lamellar structure with the  $\alpha$ -helical rod aligned parallel to the lamellar normal [Scheme 2(c)]. Based on the molecular weight of PPLG, the  $d$ -spacing of the lamellar structure (from SAXS analyses) and the length of the PPLG segment (estimated by considering the 18/5  $\alpha$ -helical conformations to have a length of 5.4 Å for each pitch of the helix),<sup>36</sup> we conclude that each PPLG domain in the bilayer structure can be formed, as supported by comparing the  $d$ -spacings of PS<sub>235</sub>-*b*-PPLG<sub>57</sub> and PS<sub>235</sub>-*b*-PPLG<sub>106</sub>, which feature the same PS block length. The difference in the lamellar spacing ( $\Delta d = 19.57 - 33.70 \text{ nm} = 14.13 \text{ nm}$ ) is close to twice the molecular length difference of PPLG ( $2 \times 49/3.6 \times 5.4 \text{ Å} = 14.7 \text{ nm}$ ). The

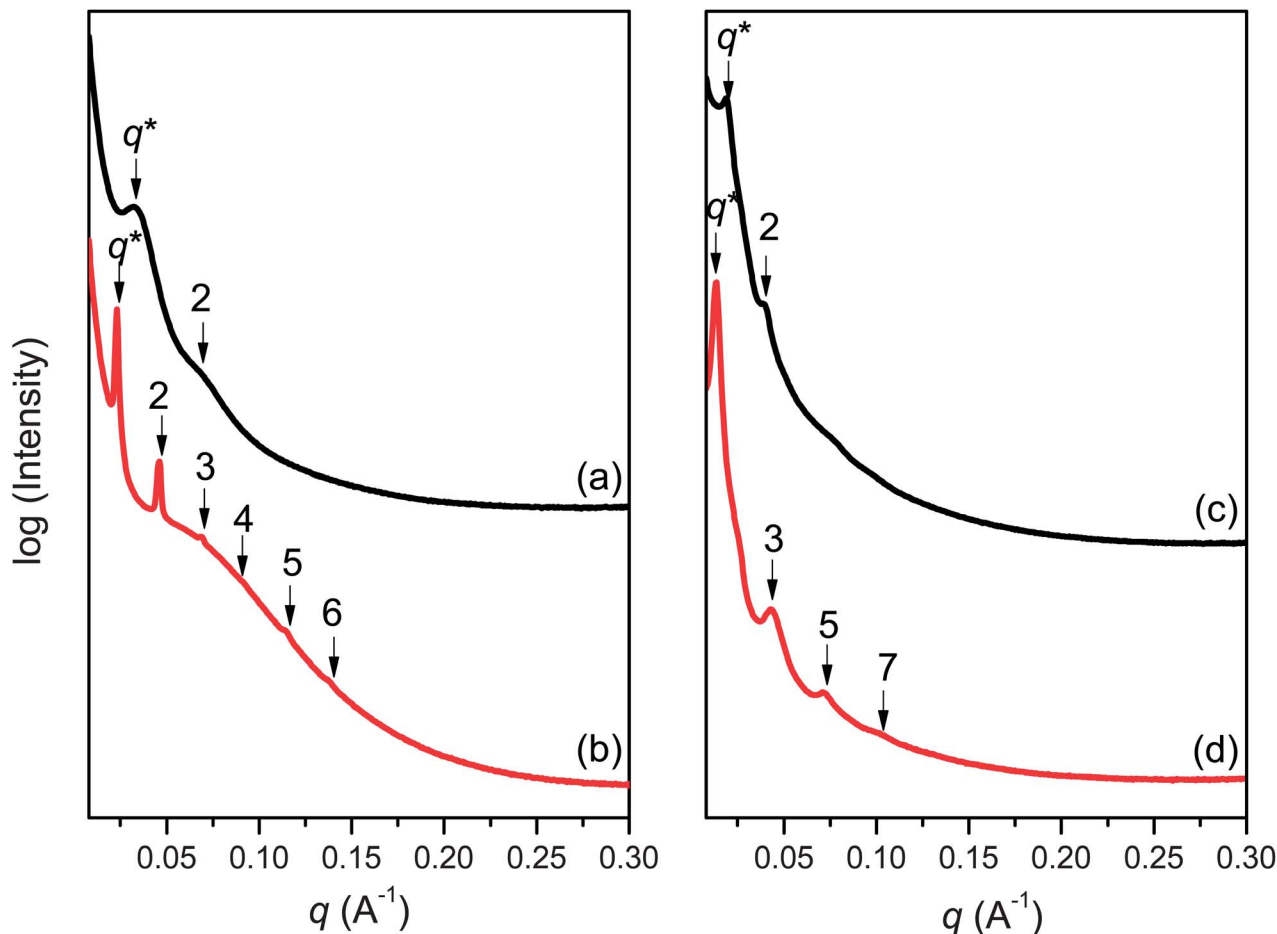


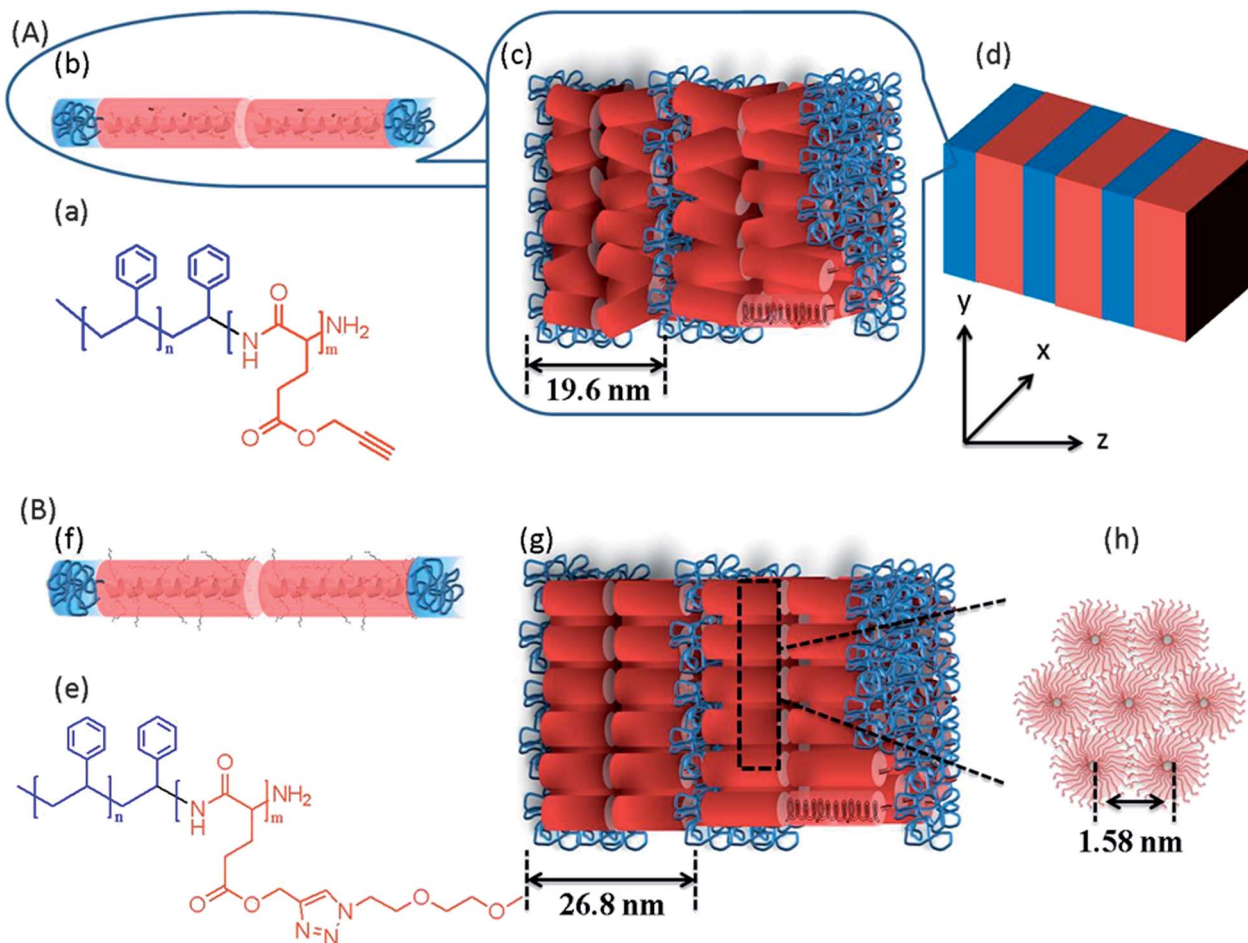
Fig. 10 SAXS patterns of (a) PS<sub>235</sub>-b-PPLG<sub>57</sub>, (b) PS<sub>235</sub>-b-(PPLG-g-MEO<sub>2</sub>)<sub>57</sub>, (c) PS<sub>235</sub>-b-PPLG<sub>106</sub>, and (d) PS<sub>235</sub>-b-(PPLG-g-MEO<sub>2</sub>)<sub>106</sub> at room temperature.

difference may come from that the PPLG did not form the long-range order of hexagonal packing cylinder as shown in Scheme 2(c) based on WAXD analysis.

We also compared  $d$ -spacings of PS<sub>235</sub>-b-(PPLG-g-MEO<sub>2</sub>)<sub>57</sub> ( $d = 26.83$  nm) with PS<sub>235</sub>-b-PPLG<sub>57</sub> ( $d = 19.57$  nm) and of PS<sub>235</sub>-b-(PPLG-g-MEO<sub>2</sub>)<sub>106</sub> ( $d = 44.88$  nm) with PS<sub>235</sub>-b-PPLG<sub>106</sub> ( $d = 33.70$  nm). Clearly, after the click reaction with MEO<sub>2</sub>-N<sub>3</sub>, the  $d$ -spacing of the lamellar structure increased. From the bottlebrushes theory, any flexible main chain can be forced to adopt an expanded rigid cylindrical conformation, due to the repulsive interaction of the densely grafted side chains, and the persistence length can be increased.<sup>53,54</sup> For example, Lecommandoux *et al.* reported that when the backbone of poly(chlorovinyl ether) was grafted with PS, the persistence length increased from 12 to 110 Å.<sup>55</sup> In addition, the lamellar structures of the PS-*b*-(PPLG-g-MEO<sub>2</sub>) copolymers were of much higher order than those of the PS-*b*-PPLG copolymers, as evidenced by the much narrower and sharper first peaks and the much greater peak ratios. For example, the PS<sub>235</sub>-b-(PPLG-g-MEO<sub>2</sub>)<sub>57</sub> copolymer featured a lamellar microdomain structure, judging from the positions of the high-order scattering maxima at the scattering vectors  $q$  of multiple integers relative to the position of the first-order scattering maximum ( $q/q_m = 1, 2, 3, 4, 5,$  and  $6$ ), as displayed in

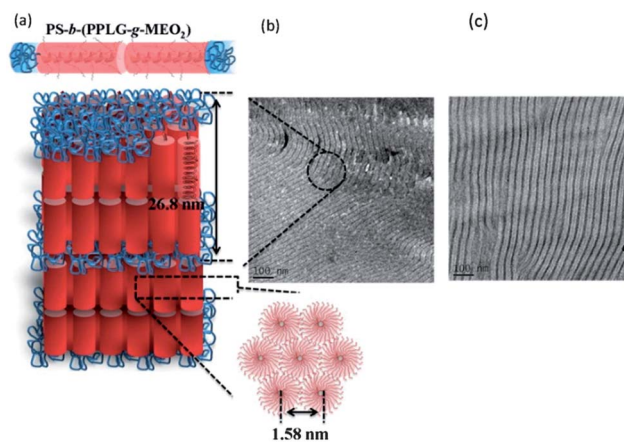
Fig. 10(b). In addition, the PS<sub>235</sub>-b-(PPLG-g-MEO<sub>2</sub>)<sub>106</sub> copolymer also possessed a lamellar microdomain structure, judging from the positions of the high-order scattering maxima at the scattering vectors  $q$  of multiple integers, but relative to the position of the first-order scattering maximum ( $q/q_m = 1, 3, 5,$  and  $7$ ), as revealed in Fig. 10(d). For a lamellar structure, the intensity of the  $n^{\text{th}}$  order peak is proportional to  $\sin^2(\pi n \Phi_a)/n^2$ , where  $\Phi_a$  (equal to  $d_a/d$ ) is the volume fraction of phase A; when the volume fractions of the two phases are equal, all even-order peaks are reduced to zero height.<sup>56</sup> Because the volume fraction of the PS segment for PS<sub>235</sub>-b-(PPLG-g-MEO<sub>2</sub>)<sub>106</sub> was approximately 0.517, which is close to 0.5, the signals for the even-order peaks (2, 4, and  $6q^*$ ) disappeared for this diblock copolymer.

Fig. 11(b) and (c) present the corresponding TEM image of PS<sub>235</sub>-b-(PPLG-g-MEO<sub>2</sub>)<sub>57</sub> and PS<sub>235</sub>-b-(PPLG-g-MEO<sub>2</sub>)<sub>106</sub>, respectively. After RuO<sub>4</sub> staining, the PS microdomains of PS-*b*-(PPLG-g-MEO<sub>2</sub>) appeared dark and the PPLG-g-MEO<sub>2</sub> microdomains appeared light, indicating the long range order of the lamellar structure. The long period distances of the lamellar structures for PS<sub>235</sub>-b-(PPLG-g-MEO<sub>2</sub>)<sub>57</sub> and PS<sub>235</sub>-b-(PPLG-g-MEO<sub>2</sub>)<sub>106</sub> were approximately 27 nm, and 44 nm, respectively, consistent with the first peak in the SAXS analysis. The length of the PS domain due to coil polymer chain ( $d_{\text{PS}} = 4$  nm) was much shorter than



**Scheme 2** (A) Schematic representation of the hierarchical structures formed from the PS-*b*-PPLG diblock copolymer: (a) and (b) chemical structures of PS<sub>235</sub>-*b*-PPLG<sub>57</sub>; (c) PPLG rods and PS coils undergoing microphase separation into a lamellar phase, with the rods aligned parallel to the layer normal and two layers of rods in each PPLG layer; (d) PS-*b*-PPLG lamellar structure. (B) Schematic representation of the hierarchical structures formed from the PS<sub>235</sub>-*b*-(PPLG-*g*-MEO<sub>2</sub>)<sub>57</sub> diblock copolymer: (e) and (f) chemical structures of PS-*b*-(PPLG-*g*-MEO<sub>2</sub>); (g) PPLG-*g*-MEO<sub>2</sub> rods and PS coils undergoing microphase separation into a lamellar phase, with the rods aligned parallel to the layer normal and two layers of rods in each PPLG-*g*-MEO<sub>2</sub> layer; (h) PPLG-*g*-MEO<sub>2</sub> blocks forming hexagonally packed cylinders.

the length of the  $\alpha$ -helical rigid rod structure of PPLG-*g*-MEO<sub>2</sub> ( $d_{\text{PPLG-}g\text{-MEO}_2} = 23$  nm), determined from the TEM image and structural considerations. Scheme 2(B) and Fig. 11(a) provide a schematic representation of the organization of the lamellar structure with  $\alpha$ -helical conformations for PS<sub>235</sub>-*b*-(PPLG-*g*-MEO<sub>2</sub>)<sub>57</sub>. The diblock copolymer formed a self-assembled lamellar structure with the peptide segments oriented perpendicular to the director of the lamellar structure. The 2D hexagonal packing of cylinders with an inter-cylinder distance of 1.58 nm for PPLG-*g*-MEO<sub>2</sub> [Scheme 2(h)], as calculated from the WAXD data, led to an average distance between the PS cylinders of 26.83 or 44.88 nm, depending on the length of the PPLG-*g*-MEO<sub>2</sub> block copolymer. Hierarchical self-assembled structures were found from these PS-*b*-(PPLG-*g*-MEO<sub>2</sub>) copolymers, including microphase separation-induced self-assembly of lamellar structures between the PS and PPLG-*g*-MEO<sub>2</sub> diblock copolymer segments and hexagonally packed cylinders of  $\alpha$ -helices from the PPLG-*g*-MEO<sub>2</sub> segment that were oriented perpendicular to the director of the lamellar structure from the diblock copolymer segments, as displayed in Scheme 2(g).



**Fig. 11** (a) The corresponding possible morphology of (b) TEM images of PS<sub>235</sub>-*b*-(PPLG-*g*-MEO<sub>2</sub>)<sub>57</sub> and (c) PS<sub>235</sub>-*b*-(PPLG-*g*-MEO<sub>2</sub>)<sub>106</sub>.

### Self-assembled structures formed from PS-*b*-(PPLG-*g*-MEO<sub>2</sub>) copolymers in solution

Because PS blocks are hydrophobic and water-insoluble and PPLG-*g*-MEO<sub>2</sub> blocks are hydrophilic and water-soluble, we expected these copolymers to undergo self-assembly into nanosized micelles with various shapes and dimensions in selective solvent systems. It is well established that changing the solvent selectivity can shift the microphase separation of block copolymers, stabilizing the disordered state or resulting in self-assembled structures ranging from spherical micelles to cylinders, vesicles, and lamellae.<sup>8–10</sup> As a general procedure, we first dissolved the block copolymer under study in a good solvent for both blocks at a typical concentration of 0.5 mg mL<sup>-1</sup>. We then added a second non-solvent, a poor solvent for one of the blocks, to the polymer solution very slowly.

Recently, Cheng *et al.* systematically studied the micellization and morphological transitions of a PS-*b*-PEO block copolymer in DMF-water and DMF-MeCN systems.<sup>19</sup> They found that the micellar morphologies were strongly dependent on the water and MeCN contents and the polymer concentration. Here, we chose these two different selective solvents (water and MeCN) to study the effects of solvents on the self-assembly of the copolymers. First, we dissolved the PS<sub>235</sub>-*b*-(PPLG-*g*-MEO<sub>2</sub>)<sub>57</sub> copolymer in the common solvent (DMF) and then added the selective solvent (MeCN) slowly to induce phase separation and aggregation of the PS block. The PS block condensed gradually with the PPLG-*g*-MEO<sub>2</sub> block constituting the outer shell of the particles. Fig. 12 presents a set of TEM images of the micelles formed from PS<sub>235</sub>-*b*-(PPLG-*g*-MEO<sub>2</sub>)<sub>57</sub> at an initial concentration of 0.5 mg mL<sup>-1</sup> in the DMF-MeCN system. Spherical micelles were formed at all MeCN concentrations; these spheres were nearly identical in size (*ca.* 20–30 nm). At the highest

MeCN concentration (90 wt%), these spherical nanoparticles were closely packed with very uniform size. We also expected the mobility of the PS blocks to be severely restricted, because MeCN is a poor solvent for PS; thus, we suspected that the morphology might not change at this highest MeCN concentration. We obtained DLS data to study the hydrodynamic diameters ( $D_h$ ) of the micelles [Fig. 11(g)]. The only single peak associated with polymer aggregates appeared as a signal near 45–55 nm for all compositions, providing direct evidence for micelle formation. The diameters of these micelles, as measured from the TEM images, were within the range 20–30 nm; these values are smaller than those measured using DLS, presumably because the preparation of the samples for TEM observation involved evaporation of the micelle particles, making chain collapse and micelle shrinkage unavoidable.

Fig. 13 presents a set of TEM images of the micelles formed from PS<sub>235</sub>-*b*-(PPLG-*g*-MEO<sub>2</sub>)<sub>57</sub> at an initial concentration of 0.5 mg mL<sup>-1</sup> in the DMF-water system. At a much relative lower water concentration of 1 wt%, the micelles were spherical and had nearly identical sizes of approximately 20–30 nm [Fig. 13(a)]. We know that these copolymers always initially form spherical micelles during the addition of water.<sup>57</sup> The hydrophilic PPLG-*g*-MEO<sub>2</sub> coronas afforded the spherical micelle solubility in water, while their hydrophobic PS cores provided locations for encapsulation [Scheme 3(a)]. Fig. 13(b)–(d) reveal that the morphologies changed to mixed spheres and short cylinders, with the population and the length of the short cylinders increasing, upon increasing the content of water (from 1.5 to 2.5 to 3.5 wt%). At a water concentration of 4 wt%, the morphology changed to long, wormlike, rod micelles [several micrometers; Fig. 13(e)]; further increasing the water concentration to 4.5 wt% resulted in the morphology changing

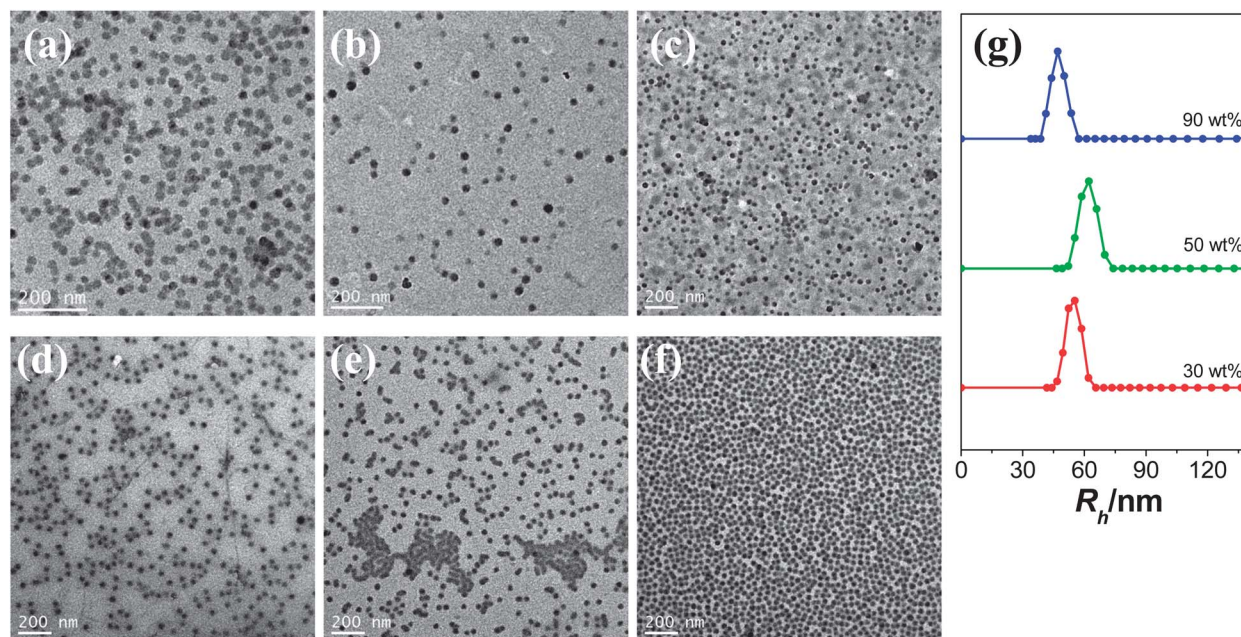


**Fig. 12** (a–f) TEM images of the PS<sub>235</sub>-*b*-(PPLG-*g*-MEO<sub>2</sub>)<sub>57</sub> block copolymer in DMF-MeCN with MeCN contents of (a) 10, (b) 30, (c) 50, (d) 70, (e) 80, and (f) 90 wt%. (g) Selected corresponding size-distributions of the micelles, as measured using DLS.

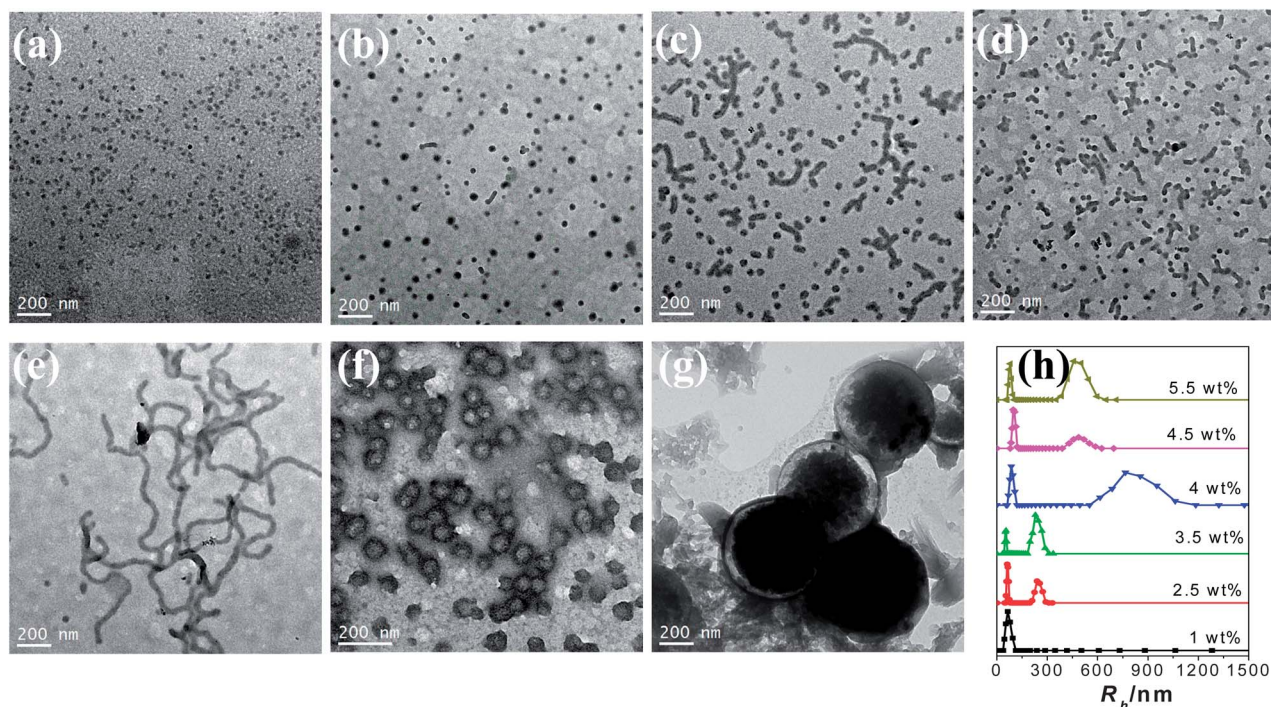
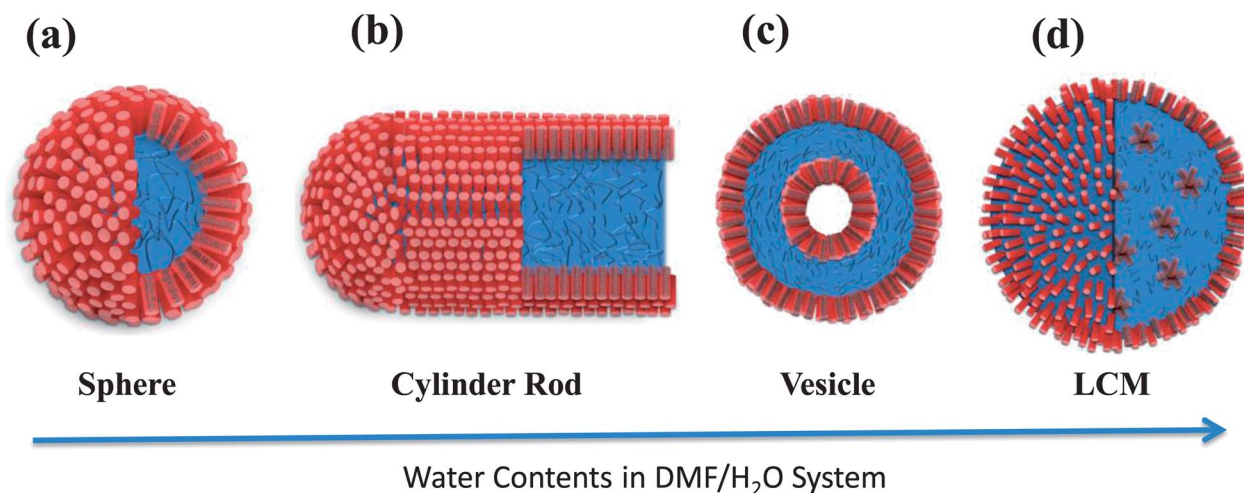


**Fig. 13** (a–g) TEM images of the  $\text{PS}_{235}\text{-}b\text{-(PPLG-g-MEO}_2\text{)}_{57}$  block copolymer in DMF–water at water contents of (a) 1, (b) 1.5, (c) 2.5, (d) 3.5, (e) 4, (f) 4.5, and (g) 5.5 wt%. (h) Corresponding size-distributions of the micelles, as measured using DLS.



**Scheme 3** Schematic representations of the morphological changes of the  $\text{PS-}b\text{-(PPLG-g-MEO}_2\text{)}$  diblock copolymer in the DMF– $\text{H}_2\text{O}$  system upon increasing the water content: (a) spherical, (b) wormlike rod, (c) vesicle, and (d) large compound micelles.

to vesicles and some large compound micelles [Fig. 13(f) and (h)]. Finally, the morphology changed to large compound micelles [Fig. 13(g)] at a water concentration of 5.5 wt%. Fig. 14 also summarizes other TEM images, possible large compound micelle scheme and DLS analyses of  $\text{PS}_{235}\text{-}b\text{-(PPLG-g-MEO}_2\text{)}_{57}$  in the DMF–water system with 5.5 wt% water content. The large compound micelle consists of an aggregation of inverse micelles, the outer surface of which is stabilized in solution by a thin layer of hydrophilic chains as clearly shown in Fig. 14(a)–(d). Fig. 13(h) displays the hydrodynamic diameters of the

copolymer structures in the DMF–water system, as analyzed using DLS. The addition of water at 1 wt% led to a single peak associated with the polymer aggregates at approximately 60 nm, a value slightly higher than that determined from the TEM image. Further increasing the water contents to 2.5 and 3.5 wt% led to a bimodal distribution at 55–65 nm and 230–240 nm for mixed spheres and short cylinders, respectively. At a water content of 4 wt%, the bimodal distribution featured peaks centered near 80 and 770 nm for long wormlike rod micelles. This bimodal distribution transformed into signals at

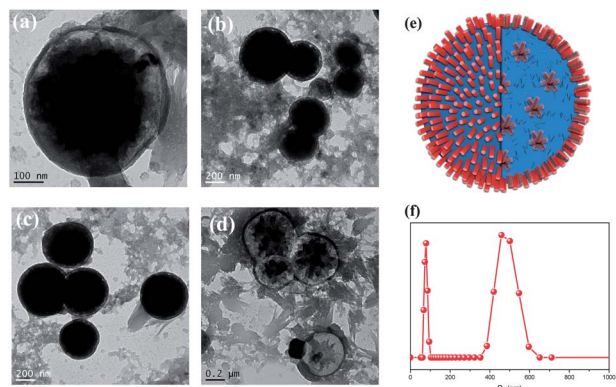


**Fig. 14** Other TEM images of  $\text{PS}_{235}\text{-}b\text{-(PPLG-g-MEO}_2\text{)}_{57}$  block copolymer in DMF–water with 5.5 wt% of water content (a)–(d), (e) scheme of large compound micelles, and (f) its corresponding size-distribution of the micelles as measured using DLS.

50–65 and 480–500 nm for vesicles and large compound micelles at water contents of 4.5 and 5.5 wt%, respectively. Clearly, the size of large compound micelles from TEM images is close to the hydrodynamic radius from DLS analyses (*ca.* 350–600) shown in Fig. 14(f).

The DLS data are consistent with the dimensions determined from the TEM images. Scheme 3 summarizes the morphological changes that occurred upon increasing the water content. Depending on the selective solvent employed, Eisenberg *et al.* reported that related aggregates transformed from spheres to rods to vesicles and, eventually, to compound micelles.<sup>57</sup> Core chain stretching, corona repulsion, and interfacial tension between the solvent and the micellar core are believed to be the main parameters dominating the formation of multi-morphological aggregates. The changes in morphology upon varying the water content can be explained by considering the change in the average number of polymer chains in an aggregate,  $N_{\text{agg}}$ . This value was small during the early stages of micellization when the copolymer chains began to form micelles. When the water content increased, the mobility of the PS chains in the core decreased and the core dimensions increased, while the total number of aggregates decreased; the total interfacial energy between the core and water would decrease, but this process would increase the degree of stretching of the PS chains in the core. Accordingly, the spheres would change to rods and then to vesicles or large compound micelles at the same critical water content to minimize the free energy as a result of decreasing the stretching penalty of the PS chains.<sup>57,58</sup> The different morphological behavior of the  $\text{PS}_{235}\text{-}b\text{-(PPLG-g-MEO}_2\text{)}_{57}$  copolymer in the DMF–water and DMF–MeCN systems was due to the very different PS–solvent interaction parameters ( $\chi$ ). The value of  $\chi_{\text{PS-water}}$  is almost nine times greater than that of  $\chi_{\text{PS-MeCN}}$ , meaning that  $\text{H}_2\text{O}$  is a much poorer solvent than MeCN for PS.<sup>19,59</sup> The increase in the interfacial free energy led to an increase in the micelle size and, thus, an increase of the stretching of the PS blocks in the cores, resulting in the spheres readily changing to form rods and then vesicles or large compound micelles in the DMF– $\text{H}_2\text{O}$  system to

minimize the free energy. We did not observe this morphological change for the  $\text{PS}_{235}\text{-}b\text{-(PPLG-g-MEO}_2\text{)}_{57}$  copolymer in the DMF–MeCN system because the relatively smaller value of  $\chi_{\text{PS-MeCN}}$  meant that a larger content of the selective solvent would be necessary to change the interfacial free energy at the critical point; we did not find this value, even when the MeCN content was 90 wt%, in this study.

## Conclusions

We have used a combination of ATRP, ROP, and click chemistry to prepare hierarchically self-assembling  $\text{PS-}b\text{-(PPLG-g-MEO}_2\text{)}$  block copolymers. After attaching EO side chains to the side chains of the  $\text{PS-}b\text{-PPLG}$  copolymers, leading to non-ionic yet water-soluble polypeptides featuring a stable  $\alpha$ -helical conformation, and greater conformation stability relative to those of the unmodified  $\text{PS-}b\text{-PPLG}$  copolymers based on FTIR spectroscopic, WAXD, and SAXS analyses. Using SAXS and TEM, we observed hierarchical self-assembly of the diblock copolymers to form lamellar nanostructures featuring  $\alpha$ -helical conformations of their polypeptide blocks. The micelle structures of the  $\text{PS-}b\text{-(PPLG-g-MEO}_2\text{)}$  block copolymers changed from spheres to rods to vesicles to large compound micelles upon increasing the water content in the DMF– $\text{H}_2\text{O}$  system, but they did not change in the DMF–MeCN system; this contrasting behavior resulted from the large difference in the PS–solvent interaction parameters ( $\chi$ ).

## Acknowledgements

This study was supported financially by the National Science Council, Taiwan, Republic of China, under contracts NSC 100-2221-E-110-029-MY3 and NSC 102-2221-E-110-008-MY3. The authors thank Mr Hsien-Tsan Lin of Regional Instruments Center at National Sun Yat-Sen University for his help in TEM experiments.

## References

- 1 S. Jain and F. S. Bates, *Science*, 2003, **300**, 460–464.
- 2 H. A. Klok and S. Lecommandoux, *Adv. Mater.*, 2001, **13**, 1217–1229.
- 3 J. Y. Cheng, A. M. Mayes and C. A. Ross, *Nat. Mater.*, 2004, **3**, 823–828.
- 4 C. J. Hawker and T. P. Russell, *MRS Bull.*, 2005, **30**, 952–966.
- 5 J. Y. Cheng, C. A. Ross, H. I. Smith and E. L. Thomas, *Adv. Mater.*, 2006, **18**, 2505–2521.
- 6 J. Rodriguez-Hernandez, F. Checot, Y. Gnanou and S. Lecommandoux, *Prog. Polym. Sci.*, 2005, **30**, 691–724.
- 7 S. Foerster and M. Antonietti, *Adv. Mater.*, 1998, **10**, 195–217.
- 8 L. Zhang and A. Eisenberg, *Science*, 1995, **268**, 1728–1730.
- 9 L. Zhang and A. Eisenberg, *J. Am. Chem. Soc.*, 1996, **118**, 3168–3181.
- 10 L. Zhang, K. Yu and A. Eisenberg, *Science*, 1996, **272**, 1777–1779.
- 11 S. C. Chen, S. W. Kuo and F. C. Chang, *Langmuir*, 2011, **27**, 10197–10205.

- 12 J. Ruokolainen, M. Saariaho, O. Ikkala, G. ten Brinke, E. L. Thomas, M. Torkkeli and R. Serimaa, *Macromolecules*, 1999, **32**, 1152–1158.
- 13 S. W. Kuo, P. H. Tung, C. L. Lai, K. U. Jeong and F. C. Chang, *Macromol. Rapid Commun.*, 2008, **29**, 229–233.
- 14 S. C. Chen, S. W. Kuo, U. S. Jeng and F. C. Chang, *Macromolecules*, 2010, **43**, 1083–1092.
- 15 C. H. Lu, F. C. Chang and S. W. Kuo, *Macromol. Chem. Phys.*, 2010, **211**, 1339–1347.
- 16 R. M. Ho, Y. W. Chiang, S. C. Lin and C. K. Chen, *Prog. Polym. Sci.*, 2011, **36**, 376–453.
- 17 R. M. Ho, C. K. Chen and Y. W. Chiang, *Macromol. Rapid Commun.*, 2009, **30**, 1439–1456.
- 18 L. Zhu, P. Huang, W. Y. Chen, Q. Ge, R. P. Quirk, S. Z. D. Cheng, E. L. Thomas, B. Lotz, B. S. Hsiao, F. J. Yeh and L. Z. Liu, *Macromolecules*, 2002, **35**, 3553–3562.
- 19 P. Bhargava, J. X. Zheng, P. Li, R. P. Quirk, F. W. Harris and S. Z. D. Cheng, *Macromolecules*, 2006, **39**, 4880–4888.
- 20 V. S. D. Voet, T. E. Pick, S. M. Park, M. Moritz, A. T. Hammack, J. J. Urban, D. F. Ogletree, D. L. Olynick and B. A. Helms, *J. Am. Chem. Soc.*, 2011, **133**, 2812–2815.
- 21 Y. C. Wu and S. W. Kuo, *Polym. Chem.*, 2012, **3**, 3100–3111.
- 22 J. G. Son, A. F. Hannon, K. W. Gotrik, A. Alexander-Katz and C. A. Ross, *Adv. Mater.*, 2011, **23**, 634–639.
- 23 Y. Z. Ni, R. Rulkens and I. Manners, *J. Am. Chem. Soc.*, 1996, **118**, 4102–4114.
- 24 S. A. Jenkkhe and X. L. Chen, *Science*, 1999, **283**, 372–375.
- 25 R. H. Lohwasser and M. Thelakktat, *Macromolecules*, 2012, **45**, 3070–3077.
- 26 S. H. Lin, S. J. Wu, C. C. Ho and W. F. Su, *Macromolecules*, 2013, **46**, 2725.
- 27 A. Yassar, L. Miozzo, R. Girona and G. Horowitz, *Prog. Polym. Sci.*, 2012, **38**, 791–844.
- 28 J. H. Hung, Y. L. Lin, Y. J. Sheng and H. K. Tsao, *Macromolecules*, 2012, **45**, 2166.
- 29 H. L. Xie, Y. X. Liu, G. Q. Zhong, H. L. Zhang, E. Q. Chen and Q. F. Zhou, *Macromolecules*, 2009, **42**, 8774–8780.
- 30 Q. H. Zhou, J. K. Zheng, Z. Shen, X. H. Fan, X. F. Chen and Q. F. Zhou, *Macromolecules*, 2010, **43**, 5637–5646.
- 31 V. K. Kotharangannagari, A. Sanchez-Ferrer, J. Ruokolainen and R. Mezzenga, *Macromolecules*, 2012, **45**, 1982–1990.
- 32 Y. S. Lu, Y. C. Lin and S. W. Kuo, *Macromolecules*, 2012, **45**, 6547.
- 33 P. Papadopoulos, G. Floudas, H. A. Klok, I. Schnell and T. Pakula, *Biomacromolecules*, 2004, **5**, 81–91.
- 34 A. Sanchez-Ferrer and R. Mezzenga, *Macromolecules*, 2010, **43**, 1093–1100.
- 35 H. F. Lee, H. S. Sheu, U. S. Jeng, C. F. Huang and F. C. Chang, *Macromolecules*, 2005, **38**, 6551–6558.
- 36 H. A. Klok and S. Lecommandoux, *Adv. Polym. Sci.*, 2006, **202**, 75–111.
- 37 S. Lecommandoux, M. F. Achard, J. F. Langenwalter and H. A. Klok, *Macromolecules*, 2001, **34**, 9100–9111.
- 38 G. Floudas, P. Papadopoulos, H. A. Klok, G. W. M. Vandermeulen and J. Rodriguez-Hernandez, *Macromolecules*, 2003, **36**, 3673–3683.
- 39 C. J. Huang and F. C. Chang, *Macromolecules*, 2008, **41**, 7041–7052.
- 40 S. W. Kuo, H. F. Lee and F. C. Chang, *J. Polym. Sci., Part A: Polym. Chem.*, 2008, **46**, 3108.
- 41 C. M. Dobson, *Nature*, 2003, **426**, 884–890.
- 42 Y. Zhang, H. Lu, Y. Lin and J. Cheng, *Macromolecules*, 2011, **44**, 6641–6644.
- 43 M. Yu, A. P. Nowak and T. J. Deming, *J. Am. Chem. Soc.*, 1999, **121**, 12210–12211.
- 44 C. Chen, Z. Wang and Z. Li, *Biomacromolecules*, 2011, **12**, 2859–2863.
- 45 A. C. Engler, H. Lee and P. T. Hammond, *Angew. Chem., Int. Ed.*, 2009, **48**, 9334–9338.
- 46 Y. Chen, C. He, C. Xiao, J. Ding, X. Zhuang and X. Chen, *Polym. Chem.*, 2011, **2**, 2627–2634.
- 47 J. Sun, G. M. Stone, N. P. Balsara and R. N. Zuckermann, *Macromolecules*, 2012, **45**, 5151–5156.
- 48 Y. C. Lin and S. W. Kuo, *J. Polym. Sci., Part A: Polym. Chem.*, 2011, **49**, 2127–2137.
- 49 Y. C. Lin and S. W. Kuo, *Polym. Chem.*, 2012, **3**, 162–171.
- 50 Y. C. Lin and S. W. Kuo, *Polym. Chem.*, 2012, **3**, 882–891.
- 51 Y. C. Lin, P. I. Wang and S. W. Kuo, *Soft Matter*, 2012, **8**, 9676.
- 52 J. Hwang and T. J. Deming, *Biomacromolecules*, 2001, **2**, 17–21.
- 53 J. Rzyayev, *Macromolecules*, 2009, **42**, 2135–2141.
- 54 J. W. Rzyayev, M. Gerle, K. Fischer and M. Schmidt, *Macromolecules*, 1996, **29**, 978–983.
- 55 S. Lecommandoux, F. Checot, R. Borsali, M. Schappacher, A. Deffieux, A. Brulet and J. P. Cotton, *Macromolecules*, 2002, **35**, 8878–8881.
- 56 R. J. Roe, *Methods of X-ray and Neutron Scattering in Polymer Science*, Oxford University Press, New York, 2000.
- 57 Y. Mai and A. Eisenberg, *Chem. Soc. Rev.*, 2012, **41**, 5969–5985.
- 58 D. E. Discher and A. Eisenberg, *Science*, 2002, **297**, 963–973.
- 59 P. Bhargava, Y. Tu, J. X. Zheng, H. Xiong, R. P. Quirk and S. Z. D. Cheng, *J. Am. Chem. Soc.*, 2007, **129**, 1113–1121.